Structural and physicochemical properties of nickel manganite NiMn$_2$O$_{4-\delta}$ synthesized by sol-gel and ultra sound assisted methods

D. Alburquenque [a, b], L. Troncoso [c], J.C. Denardin [c], A. Butera [d], K.D. Padmasree [e], J. Ortiz [a], F. Herrera [a], J.F. Marco [f], J.L. Gautier [a, *]

[a] Materials Chemistry Department, USACH, Ave L.B.O'Higgins 3363, Santiago 9170022, Chile
[b] Metallurgy Department, USACH, Ave Ecuador 3469, Santiago 9170124, Chile
[c] Physics Department, USACH, Ave. Ecuador 3493, Santiago 9170124, Chile
[d] Atomic Center, CNEA, Ito. Balseiro, Bariloche Rio Negro 84000, Argentina
[e] Cinvestav, U.Saltillo, Monterrey Km 13.5, Saltillo CP 25900, Mexico
[f] Institute of Physical Chemistry "Rocasolano", CSIC, Serrano 119, Madrid 28006, Spain

ARTICLE INFO

ABSTRACT

In this work we present the structural, magnetic and surface characterization of the ceramic nickel manganite oxide NiMn$_2$O$_{4-\delta}$ synthesized by two methods: sol-gel and ultrasound-assisted sol-gel using nitrate salts as precursors. We have characterized the non-stoichiometric samples NiMn$_2$O$_{4-\delta}$ using different physicochemical analyses. X-ray diffraction and Rietveld refinement of the X-ray data indicated that the samples crystallize in the Fd3m space group characteristic of cubic spinel-related oxides. The specific surface area of the oxides was 1.3 m^2/g (SG) and 16.3 m^2/g (UASG). SEM results showed particle agglomerates of 1.05 μm (SG) and 0.85 μm (UASG). Temperature dependence magnetization measurements were performed and a ferrimagnetic transition was identified at 103 K and 105 K depending on the preparation method (SG and UASG, respectively). The observed Curie constant was found to vary from 7.4 to 7.7 cm^3 K mol^{-1} and hysteretic magnetization vs. applied field curves at different temperatures were obtained. XPS studies of these oxides reveal the presence of Ni^{2+}, Mn^{2+}, Mn^{3+} and Mn^{4+} ions at the surface. A probable ionic distribution as a function of the synthesis method is proposed.

© 2016 Elsevier B.V. All rights reserved.

1. Introduction

Spinel manganese mixed oxides display promising applications in several areas, such as optics, electronics, biology, medicine, etc. due to their particular electrical and magnetic properties, which arise from the mixed valence states of manganese. The spinel structure can adopt three types of cation configurations. The first arrangement is known as normal spinel, with the formula (A)[B$_2$]O$_4$ where (A) denotes a cation A occupying the tetrahedral sites, and therefore having four oxygen's as nearest neighbors, while [B] denotes an octahedral site occupied by two B cations having six oxygen atoms as nearest neighbors. A second arrangement-known as a perfectly inverted spinel-can be formulated as (B)[AB]O$_4$ where (B) denotes a cation B in oxygen tetrahedral coordination, and [AB]

denotes an equal number of A and B cations in octahedral positions. There are also other possible intermediate distributions represented by the formula (A$_{1-\nu}$B$_\nu$)[A$_\nu$B$_{1-\nu}$]O$_4$, where ν denotes the inversion degree, which usually is affected by the preparation conditions used in the synthesis. Considering the relative complexity of the cation distributions, any research in spinels must take into account the intrinsic dichotomy among the tetrahedral and octahedral sites, and the possibility that the cations can adopt two, or three, different oxidation states within the same oxide, giving rise to different ordered states and then modifying the mechanisms of electrical transport [1–3].

Among the materials with spinel structure, nickel manganite NiMn$_2$O$_4$, which is well-known since long time [4,5], shows a partially inverse cubic spinel structure Ni$_{1-\nu}$Mn$_{1-\nu}$[Ni$_\nu$Mn$_{2-\nu}$]O$_4$, where ν determines both its structural and electrical properties [6]. This oxide is widely used for the production of ceramics temperature sensors due to its negative temperature coefficient of the electrical resistance [7]; it has been also investigated as a possible electrochemical capacitor [8,9] as well as electrocatalyst

[10]. NiMn$_2$O$_4$ has been synthesized in the form of powders, films, thick films and single crystals. From the technical point of view, solid-state reaction between simple oxides, thermal calcination using organic and inorganic precursors [11–17], as well as ball milling [18] and sol–gel [19] techniques have been the principal routes used for powder synthesis. In most of these methods, high temperatures and prolonged time of sintering are usually necessary. For NiMn$_2$O$_4$, several cation configurations have been proposed in the literature, which appear to depend upon the synthesis conditions [20–37]. Different cations may occupy either the A-sites or the B-sites or both, depending on their oxidation states and their ionic radii, according with their energetic preference, giving rise to two different sublattices A and B connected through oxygen ions. The presence of these sublattices having metals in different oxidation states may lead to long range magnetic and conducting interactions of the type M^{n+}-O-M^{n+1}. In fact, the presence of the M^{n+1}/Mn^{n+} redox couple located in B-sites of the semiconductor spinel has been considered as the responsible factor of the controlled-valence conduction mechanism proposed by Verwey [38]. As an example, different cationic distributions $[Ni_{0.1}^{2+}Mn_{0.9}^{3+}][Ni_{0.9}^{2+}Mn_{1.1}^{3+}]O_4^{2-}$ [30], $Mn^{3+}[Ni^{2+}Mn_{0.1}^{2+}Mn_{0.9}^{3+}]O_{3.95}^{2-}$ [24], $Mn_{0.65}^{2+}Mn_{0.35}^{3+}[Ni^{2+}Mn_{0.35}^{3+}Mn_{0.65}^{4+}]O_4^{2-}$ [22] have been proposed for NiMn$_2$O$_4$. The mixed-valence Mn-ions together with Ni^{2+} ions and the oxygen anions could lead to different magnetic interactions, between Mn^{2+}–O^{2-}–Mn^{3+}, Mn^{3+}–O^{2-}–Mn^{3+}, and Mn^{3+}–O^{2-}–Mn^{4+} pairs. Recent works on spinel manganite have shown that the broad magnetic behavior is conditioned by the complex cation distributions, and, additionally, both the morphology and particle size, as well as the oxygen stoichiometry, appear to play an important role at this respect [39–41]. On the other hand, four magnetic phase transitions have been observed recently from magnetization-temperature measurements [42].

In order to obtain a better understanding of the effect of the preparation method on the relative cation configuration of these spinel oxides, we have performed a systematic study of the physico-chemical properties of NiMn$_2$O$_{4-\delta}$ synthesized by two closely-related methods: sol-gel and ultrasound-assisted sol-gel. We report herein our main observations performed using X-ray diffraction techniques, scanning electron microscopy and EDS analyses, BET surface area measurements, oxygen stoichiometry determinations, XPS measurements and magnetic studies.

2. Experimental

2.1. Synthesis of NiMn$_2$O$_4$

The chemical synthesis of NiMn$_2$O$_4$ was conducted by an acid citric sol–gel route (SG), and by ultrasonic assisted sol–gel route (UASG) using the sonochemical method. We have used nickel and manganese nitrate salts as precursors. The ratio of metals in the oxides was checked using atomic absorption spectroscopy.

Synthesis by the sol–gel method [43]: The starting point of the synthesis procedure was the formation of a citrate–based precursor from nickel nitrate hexahydrate (Ni(NO$_3$)$_2$ × 6 H$_2$O, Sigma–Aldrich ≥ 98%) and manganese nitrate tetrahydrate (Mn(NO$_3$)$_2$ × 4 H$_2$O Sigma–Aldrich ≥ 98%). The reagents were diluted in water taking into account the stoichiometric ratio Mn/Ni = 2. Citric acid was added into the solution until the molar ratio between the metal (Ni, Mn) ions and citric acid was 1:4. The solution was stirred at RT for 1h, and then neutralized by ammonia. Ethylene glycol (Fluka p.a.) was used as polymerization agent in the molar ratio metal-ions: ethylene glycol = 1:9. The obtained mixture was stirred first at 60 °C to evaporate water and increase the viscosity and then at 90 °C for 1 h until a transparent sol was obtained.

Then the solution was heated at 120 °C, to create a gel which slowly turned into a dark resin. Subsequently, the temperature was increased to 200 °C for 12 h to remove the organic components.

The resulting precursor gel was calcined in a furnace at 950 °C for 24 h in oxygen atmosphere. The heating rate was fixed at 10 °C/min. A black powder was obtained as final product.

Synthesis by the sonochemical method [44]: The precursors employed were the same used on the preparation of the sol–gel method. The sol–gel synthesis assisted by ultrasound consists of the following two stages:

First stage: In a 200 mL beaker, stoichiometric amounts of precursors in the Ni/Mn = 1/2 atomic ratio were dissolved in 100 mL water and then the solution was agitated on a hotplate for 15 min. After this time, 5 mL of ethylene glycol were added to obtain a homogeneous solution. Subsequently, the reaction vessel was placed in the ultrasound equipment (Sonic Vibra Cell VCX750), at 750 W and 20 KHz for 1 h. After 5 min, 5 g of citric acid were added under vigorous stirring. Then, the reaction vessel was placed in a furnace at 95 °C for 12 h in order to remove water.

Second stage: the pasty material obtained was then poured in an alumina crucible and calcined at 800 °C for 6h in oxygen at a heating rate of 2 °C/min. A black powder was obtained as final product.

2.2. Characterization techniques

X-ray patterns of the synthesized NiMn$_2$O$_{4-\delta}$ powders were collected on a Shimadzu 6000 diffractometer, controlled by a Shimadzu 6000 software, operating at 40 kV and 30 mA in Bragg-Brentano reflection geometry with CuKα radiation (λ = 1.5418 Å), using a 2θ range 10°–90° and a scanning rate of 2° min^{-1}. For Rietveld refinement analysis [45], XRD patterns were recorded over long periods (24h) and fitted using the FULLPROF program [46]. A pseudo-Voigt function was chosen to simulate the line shape of the diffraction peaks. The following parameters were refined in the final run of the fit: scale factor, background coefficients, zero-point error, unit–cell parameters, pseudo-Voigt profile corrected for asymmetry parameters and positional coordinates. The average size of the particles was estimated using the Debye-Scherrer formula according with a methodology already published [47].

Sample morphology and grain sizes were examined by means of scanning electron microscopy (SEM) using a Zeiss EVO MA10 apparatus and an acceleration voltage of 20 keV. The microscope was equipped with an Oxford X-Act EDS for quantitative characterization. The samples were observed without coating and the EDS was previously calibrated with a Cu standard.

Specific surface measurements were carried out by using the BET method and the nitrogen adsorption isotherm at 77 K was determined volumetrically after outgassing at 1 × 10^{-5} Torr for 30 min at 350 °C (Quantachrome model AS-1 CT-8 apparatus). The nickel manganite samples were outgassed previously at 1 10^{-5} Torr for 30 min at 350 °C.

The oxidation power (z) was determined by chemical reduction of the oxide cations M^{n+} with n ≥ 3 to n = 2 using a soft reduction agent, such as 0.04N VOSO$_4$ in sulfuric solution according to reaction 1. In this method, approximately 60 mg of oxide were mixed with 50 mL of VOSO$_4$ and the mix was heated at 90 °C for 24 h. After the oxide dissolution, the VOSO$_4$ excess was potentiometrically titrated with a 0.0626N KMnO$_4$ standardized solution. Oxidation power was calculated according to the equation [36]: z = [(V$_{VO}$N$_{VO}$−V$_K$N$_K$)M$_{ox}$]m$_{ox}$ where V$_{VO}$ and N$_{VO}$ and V$_K$ and N$_K$ are the volume and concentration of VOSO$_4$ solution and KMnO$_4$ solution respectively, and M$_{ox}$ and m$_{ox}$ are the molar mass and weight of oxide, respectively. Three determinations were made for each sample.

$$(NiMn_2)^{z+} + (z-6)VO^{2+} + 3(z-6)H_2O \rightarrow Ni^{2+} + 2Mn^{2+}$$
$$+ (z-6)V(OH)_4^+ + 2(z-6)H^+ \qquad (1)$$
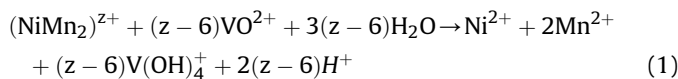
The magnetic measurements recorded from both preparations of nickel manganite were performed with a SQUID magnetometer (Quantum Design model MPMS XL5) in the temperature range 5–300 K under a magnetic field of 100Oe, in both field cooled (FC) and zero-field-cooled (ZFC) modes. Magnetization data as a function of applied field were recorded at 5 K and 300 K from both the SG and UASG samples using a cryogenic vibrating magnetometer (Cryogenic 5T VSM). Hysteresis curves were measured in the range ±30 kOe at fixed temperatures. The VSM was previously calibrated with a pure standard YIG sphere. Samples were measured in powder form, compacted into pellets and placed inside a gelatine capsule of negligible magnetic contribution.

In order to determine the magnetic moment μ_{eff}, magnetic susceptibility measurements were performed in the temperature range 298 K–1173 K, using a Faraday type magnetic balance in a constant field of 5 KOe. Data were acquired both in the heating and cooling cycles and averaged in order to correct for a small thermal hysteresis.

The oxides surface composition was examined by X-ray photoelectron spectroscopy (XPS). XPS spectra were recorded with a PHOIBOS-150 electron analyzer under an operating vacuum below 7×10^{-10} mbar, using Mg Kα radiation (1253.6 eV) and a constant pass energy of 200 eV and 20 eV for the wide scan and narrow scan spectra, respectively. All binding energies (BE ± 0.2 eV) were charge−corrected to the C 1s signal of the adventitious contamination carbon layer, set at 284.6eV. All the spectra were computer-fitted using a program based on procedures described in the literature [48].

3. Results and discussion

3.1. X-ray diffraction and rietveld refinements

The crystal structures of the samples were investigated using XRD. Fig. 1 displays the calculated intensity and experimental XRD patterns for the SG and UASG samples. The peaks shown in the XRD pattern are sharp and intense, indicating good crystallinity of the particles. From the fifteen reflections identified, the principal diffraction peaks of $NiMn_2O_{4-\delta}$ can be assigned to the (111), (220), (311), (222), (400), (422), (511) and (440) planes. No other peaks of impurities were found in the XRD patterns. The results indicate that samples crystallized in the pure spinel structure, with a lattice parameter of 8.4090 Å (SG) and 8.3969 Å (UASG). These values are in good agreement with values reported in the literature (a = 8.382 Å, ICDD-card 01-1110 and a = 8.450 Å, ICDD-card 71-0852) [49]. We have performed Rietveld refinement analysis using the cubic Fd3m space group. Crystal data for SG and UASG samples are summarized in Table 1. Assuming an inverse spinel structure, we have placed in 8a positions the Ni^{2+} y Mn^{2+} ions while Ni^{2+}, Mn^{3+}, Mn^{4+} ions have been located in 16d positions. The O^{2-} anions position are in the 32e site with x-coordinates values of 0.26048 and 0.25943 for the SG and UASG samples, respectively. The OCC factor values for the Ni^{2+}_{8a}, Mn^{2+}_{8a}, Ni^{2+}_{16d}, Mn^{3+}_{16d}, Mn^{4+}_{16d} and O^{2-}_{32e} ions were 0.00625, 0.03542, 0.03542, 0.025, 0.025 and 0.0229, respectively for the SG samples and 0.0104, 0.0313, 0.0313, 0.0171, 0.025 and 0.1635, respectively for the UASG samples. The (311) peak of $NiMn_2O_{4-\delta}$ was further analyzed by fitting it to a Gaussian distribution to obtain its FWHM. The average crystallite size was calculated using the Scherrer equation [47]. It was found to be 11 nm for the SG sample and 7 nm for the UASG sample.
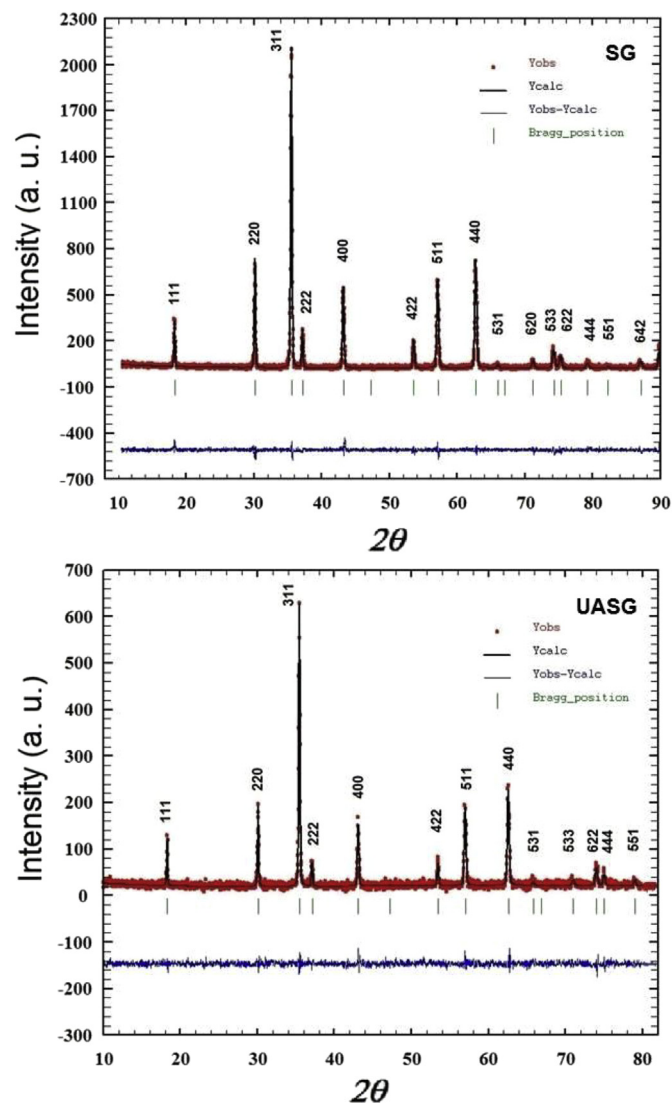

Fig. 1. Rietveld results. Observed and calculated XRD profiles of $NiMn_2O_{4-\delta}$ SG and UASG samples.

Table 1
Crystal data from Rietveld refinement.

Phase	$NiMn_2O_{4-\delta}$ SG	$NiMn_2O_{4-\delta}$ UASG
Crystal System	Cubic	Cubic
Space Group	Fd3m	Fd3m
a (A°)	8.36876 ± 0.00043	8.38664 ± 0.00081
V (A°³)	586.516	589.880
R_B	5.44	6.82
R_F	4.76	6.74
R_P	22.8	13.4
R_{WP}	24.5	17.2
R_{exp}	18.4	17.54
χ^2	1.78	0.959

The specific surface area of the oxides was determined using nitrogen adsorption at 77 K. The isotherm belongs to the type II of BET's classification. S_{BET} data of 1.3 m²/g (SG) and 16.3 m²/g (UASG) correspond to spheres with diameters of 750 and 60 μm, respectively.

3.2. Morphology and oxygen stoichiometry

The microscopy observation of the $NiMn_2O_{4-\delta}$ powders obtained from the SG and UASG methods shows submicron particles of irregular morphology that form agglomerates of several micrometers in diameter (Fig. 2). From Fig. 2, the size of the agglomerates can be estimated to be 1.05 μm (SG) and 0.85 μm (UASG). This important difference with respect to BET results is due at two factors: large particles agglomeration and irregular shape.

The atomic Mn/Ni ratios obtained from EDS measurements were very similar for both types of materials: 2.25 (SG) and 2.27 (UASG). The oxygen contents in both samples are again similar, being 56.1% for SG and 57.4% for UASG (Fig. 3). There is always an error associated to the quantitative analysis by EDS, particularly in the oxygen determination as it has been reported in the literature [17,41]. The relative variation in metals and oxygen stoichiometry was confirmed by using wet chemical methods, which are much more appropriate to determine manganese valence fluctuations. From those fluctuations and by charge equilibrium arguments, it was possible to determine the oxygen content in the materials. The global oxidation degree results determined using the redox titration technique with vanadyl sulfate are shown in Table 2. We assumed that all nickel was present as Ni^{2+}. The results indicate

that the stoichiometry of each oxide can be written in the form: $Ni(Mn^{2+})_{0.85}[Mn^{4+/3+}]_{1.15}O_{3.85}$ for SG and $Ni(Mn^{2+})_{0.75}[Mn^{4+/3+}]_{1.25}O_{3.93}$ for UASG preparations. On the other hand, these results are in good agreement with the measurements obtained from EDS analyses.

3.3. Magnetic measurements

In manganese-based oxides, the exchange interactions between the manganese ions lead to a variety of magnetic states with different properties such as ferromagnetic, antiferromagnetic, ferrimagnetic and spin glass. Manganese ions may have bivalent Mn^{2+}, trivalent Mn^{3+} and tetravalent Mn^{4+} states, whereas nickel is only bivalent Ni^{2+} in $NiMn_2O_{4-\delta}$. The temperature dependence of the magnetization of the non-stoichiometric $NiMn_2O_{4-\delta}$ system (SG and UASG samples) was investigated using an applied magnetic field of H = 100 Oe for ZFC and FC modes, performed from 5 K to 300 K employing a SQUID magnetometer. ZFC and FC denote the magnetization in the cooling run under zero magnetic field and the cooling run under magnetic field, respectively. Fig. 4 shows the thermal dependence of the magnetization of $NiMn_2O_{4-\delta}$ for both preparation methods. Two magnetic transitions are observed: at high temperatures, the paramagnetic–ferrimagnetic transitions at Tc, characterized by a sudden increase of the magnetization when the temperature decreases and, at lower temperatures where the possible existence of a collinear Néel state, as pointed out by Ma et al. [50], might occur. The ferrimagnetic transition was observed at T_C = 103 K and T_C = 105 K for SG and UASG, respectively. The decrease in T_C can be related to the reduction of the crystallite size or to the effect of oxygen vacancies, as discussed by Lisboa-Filho et al. [41]. The transition at 105 K was also observed for the $NiMn_2O_4$ powder prepared at 1000 °C [51]. However, Asbrinket al. [16] using a single crystal, observed T_C = 145 K whereas Nelson-Cheeeman et al. [52] reported 110 K in $NiMn_2O_4$ thin films. It is known that ferrimagnetic behavior has been observed in compounds with different 3d-ions or comporting one type of magnetic ion in different crystallographic positions. In Fig. 4 a large difference between ZFC and FC is observed.

In the ZFC mode, a first broad maximum occurs at about 66 K followed by an antiferrimagnetic-type transition at 91 K for the SG sample. In the case of the UASG sample, a shoulder is detected at 64 K followed by a maximum at 87 K. Such double-transition feature has been already observed [42,53]. During the FC procedure, the magnetization increases monotonically for both samples, as already reported [54]. Our results reflect the presence of a complex magnetic structure with existence of several magnetic sublattices in the oxides. At low temperature the Mn^{2+}- Mn^{3+} or Mn^{3+}- Ni^{2+} antiferromagnetic interactions are relevant, while at higher temperature close to the magnetic transition at 105 K, Mn^{3+} and Mn^{4+} ferromagnetic interactions would be important [41]. The competition between ferromagnetic (F) and antiferromagnetic sublattices (AF) leads to a ferrimagnetic-like state as we had already proposed [55,56]. The interaction between Ni^{2+} and Mn^{3+} ions has been suggested to be ferromagnetic [53]. Additionally Ni–O–Ni interactions may also play a role.

Fig. 5 shows the magnetization behavior measured at 5 K and 300 K with increasing and decreasing applied magnetic field from both the SG and UASG samples. The dependence of magnetization with applied magnetic field at 300 K shows a paramagnetic behavior in both samples, behavior that can be associated to small particles, as it has been shown in the SEM images and from the XRD Scherrer analysis. At 5 K a typical ferromagnetic behavior is observed, with a saturation magnetization of 28 emu/g, and coercivity fields of Hc = 94Oe for the SG sample and Hc = 31Oe for the UASG sample, as can be seen in the inset of Fig. 5. As it is observed in
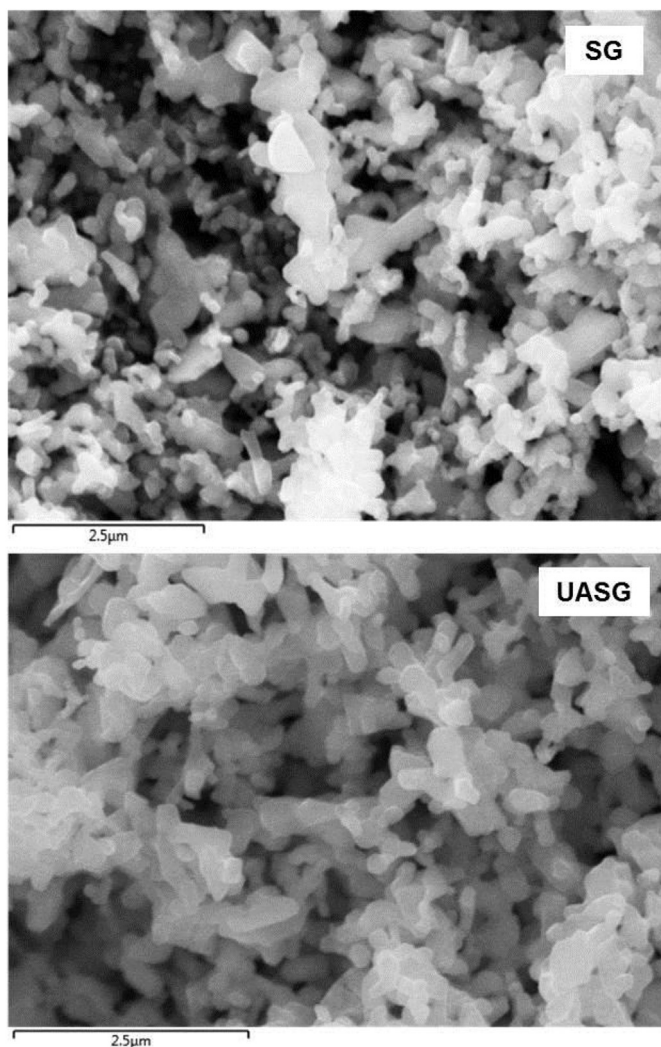

Fig. 2. Scanning electron micrographs of representative nickel manganite powders obtained by SG and UASG method.
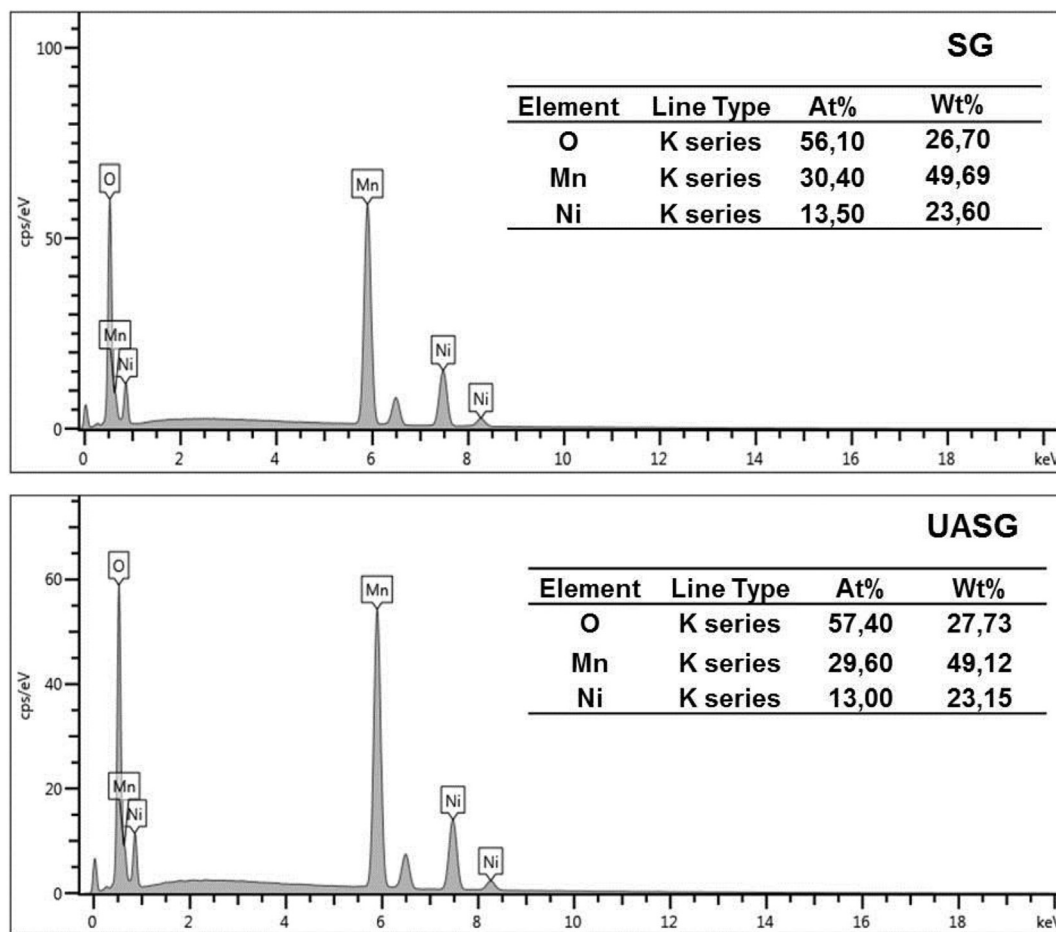
Fig. 3. X-ray energy dispersive spectra (EDS) recorded from nickel manganite powders obtained from SG and UASG preparations. The inset shows the values of weight and atomic percentages obtained for the samples.

the hysteresis curves at 5 K, the UASG sample has a higher coercivity than the SG sample. The increase of coercivity at low temperatures can be an indicative of the presence of superparamagnetic nanoparticles in the UASG sample. The coercivity of UASG sample was observed to increase continuously as temperature decreases from 100 K to 5 K, what is a typical behavior of small magnetic nanoparticles below their blocking temperature [57]. In the case of SG sample, the coercivity is almost constant in the lower temperature regime, and only decreases around 100 K, near the critical temperature Tc. Concerning the remanent magnetization, M_r, SG sample shows $M_r = 10$ emu/g whereas for UASG sample $M_r = 15$ emu/g.

Molar magnetic susceptibilities as a function of temperature (paramagnetic regime) are presented in Fig. 6 for the SG and UASG samples. The behavior of $1/\chi$ was reproducible for all samples. The temperature range explored was 300–800 K. The magnetic susceptibility obeys a Curie–Weiss law $\chi = C/(T-\Theta) + \chi_{TIP}$, considering a temperature-independent contribution ($\chi_{TIP} \sim 10^{-3}$ emu K/mol). The experimental values of μ_{eff}, Curie constant, Curie temperature and Curie–Weiss temperature are shown in Table 3.

3.4. XPS measurements

The survey XPS spectra (not shown) recorded from compounds of composition $NiMn_2O_4$ either prepared by SG or UASG are similar, showing the expected Ni, Mn, O and C contributions. The Ni 2p XPS spectra recorded from both samples were all very similar. Fig. 7

shows a representative Ni 2p spectrum (SG sample). The binding energy of the main photoemission Ni $2p_{3/2}$ line (854.6eV) and that of the corresponding shake-up satellite (861.0eV) are compatible with the presence of Ni^{2+} [58]. The Mn 2p spectra recorded from the two nickel manganites show a quite broad spin–orbit doublet (Fig. 8). The binding energies of the Mn $2p_{3/2}$ and $2p_{1/2}$ levels were in both cases 641.6 eV and 653.3 eV, respectively. These binding energies are close to those shown by Mn^{3+} [59].

It is well-known that the Mn 2p spectra of Mn oxides contain many contributions due to the occurrence of multiplet splitting. Therefore, in the case of the coexistence of various oxidation states of Mn in a sample, it is very difficult to distinguish, given the strong overlap between all peaks, the main photoemission signals

Table 2
Global oxidation degree z determined using chemical reduction reaction with 0.04N $VOSO_4$ (50 mL).

Sample	Mass (mg)	V (mL) $KMnO_4$ 0.0626 N	z (eqmol^{-1})
SG	62.2	24.95	3.82
	60.4	24.75	3.87
$Ni_{0.15}Mn_{0.85}[Ni_{0.85}Mn_{1.15}]$	60.0	24.85	3.86
$O_{3.85}$		$\bar{x}$	3.85
UASG	63.1	24.15	3.90
	61.5	23.95	3.95
$Ni_{0.25}Mn_{0.75}[Ni_{0.75}Mn_{1.25}]$	62.1	24.05	3.93
$O_{3.93}$		$\bar{x}$	3.93
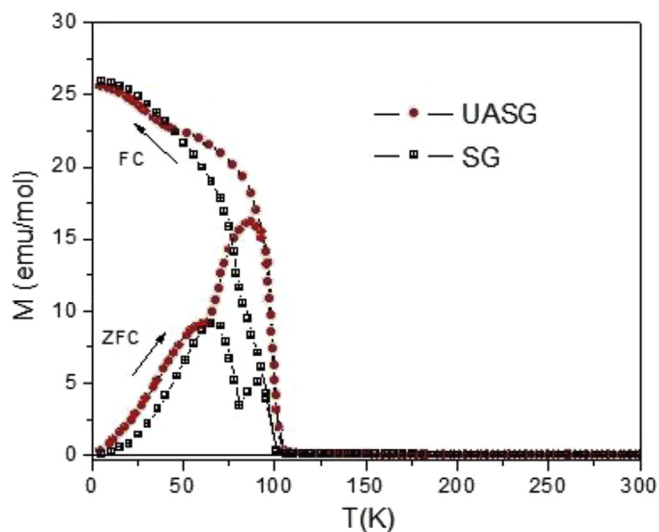
Fig. 4. Zero field cooling (ZFC) and field cooling (FC) curves for UASG and SG samples measured at 100 Oe.
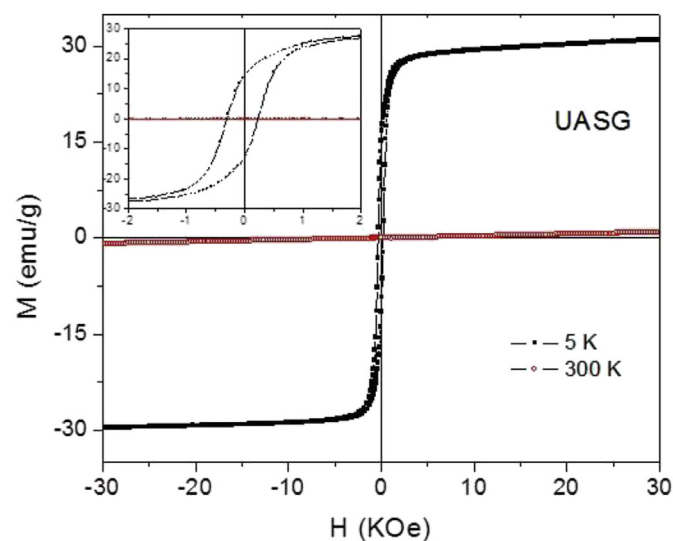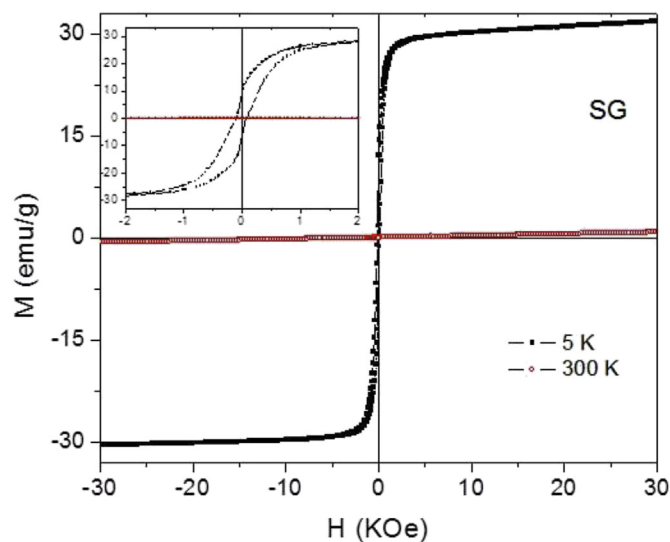

Fig. 5. Magnetization as function of applied magnetic field at 5 K and 300 K recorded from SG and UASG samples. The inset shows a zoom of the curves at 5 K where the coercivity field can be observed.

corresponding to a particular Mn oxidation state from the multiplet splitting components due to another different oxidation state. Although the position of the main Mn $2p_{3/2}$ and Mn $2p_{1/2}$ core levels can give an idea of the average oxidation state, it results very complicated to quantify the different contributions corresponding to each one of the possible Mn oxidation states which could be present in the sample. It is well-known that in the case of Mn^{2+}, the Mn 2p spectra present a clear shake up satellite around 6.0 eV above the main Mn $2p_{3/2}$ photoemission peak. However, in the event that Mn^{2+} is not in an abundant concentration this satellite would be diluted in the high binding energy side of the Mn $2p_{3/2}$ line and, rather than a satellite itself, it would appear as an asymmetry in that part of the spectrum. In the case of the two samples considered in this paper, the Mn 2p spectra are very similar (Fig. 8) and the binding energies of their respective Mn $2p_{3/2}$ and the Mn $2p_{1/2}$ core levels point out, as mentioned above, to an average oxidation state of Mn^{3+}. In order to determine the oxidation state of Mn it appears more reliable to use the Mn 3s spectra. Due to the occurrence of multiplet splitting, the Mn 3s peak, which should be a singlet as it corresponds to an electronic level with $l = 0$, splits into two peaks herein after denoted as Mn 3s(1) and Mn 3s(2) (in this notation the term Mn 3s(1) will refer to the more intense peak appearing at lower binding energy and the Mn 3s(2) will refer to the less intense peak appearing at higher binding energy) (Fig. 9). Both the binding energy (BE) of the Mn 3s(1) peak, and above all, the energy difference ΔE_{3s} between Mn 3s(2) and Mn 3s(1) are absolutely characteristic of each of the possible oxydation states of Mn. So, for Mn^{2+}, BE (Mn 3s(1)) = 82.6 eV and $\Delta E_{3s} \sim 5.9$ eV. For Mn^{3+}, BE (Mn 3s(1)) = 83.4 eV and $\Delta E_{3s} \sim 5.4$ eV while for Mn^{4+} BE (Mn 3s(1)) = 84.4 eV and $\Delta E_{3s} \sim 4.8$ eV.

Beyreuther et al. [60] after studying by XPS numerous Mn compounds, derived the following equation to calculate the average valence of Mn from the ΔE_{3s} value: $V_{Mn} = 9.67 - 1.27 \Delta E_{3s}$

According to this equation, and taking into account that the ΔE_{3s} energy difference for the SG and USAG samples was 5.42 and 5.34, respectively, we obtained the following values V_{Mn} for the two samples considered in this work: 2.79 and 2.89.

Thus, the results indicate that the average oxidation state of Mn in these samples is close to 3+, but not strictly 3+. This suggests the existence of Mn species in more than one oxidation state in these samples.

If we observe the Mn 3s reference spectra reported in the literature [61,62] for MnO, Mn_2O_3 and MnO_2 it can be noted that they are constituted by two relatively symmetric peaks (in the following we will call these two peaks "doublet" taking into account that its origin is due to multiplet splitting and does not correspond to a genuine spin−orbit doublet) having, in practice, the same width. Given that when the oxidation state of Mn increases the Mn 3s(1) peaks shifts significantly to higher binding energies and that, on the contrary, the separation ΔE_{3s} decreases noticeably, in the case of coexistence of several oxidation states of Mn, the final Mn 3s spectrum would be constituted by a broad Mn 3s(1) peak (even asymmetric depending on the weight of the different contributions) and a much narrower Mn3s(2) peak. In the present work we have a situation similar to this. A Mn 3s(1) peak quite asymmetric and broad, and a much narrower Mn 3s(2) peak. This suggests the coexistence of more than one oxidation state of Mn.

We have used several fitting models considering different situations: coexistence of Mn^{4+} and Mn^{2+} and coexistence of Mn^{4+}, Mn^{3+} and Mn^{2+}. The final decision of adopting one or another fitting model is not straight forward since the usual χ^2 criterion
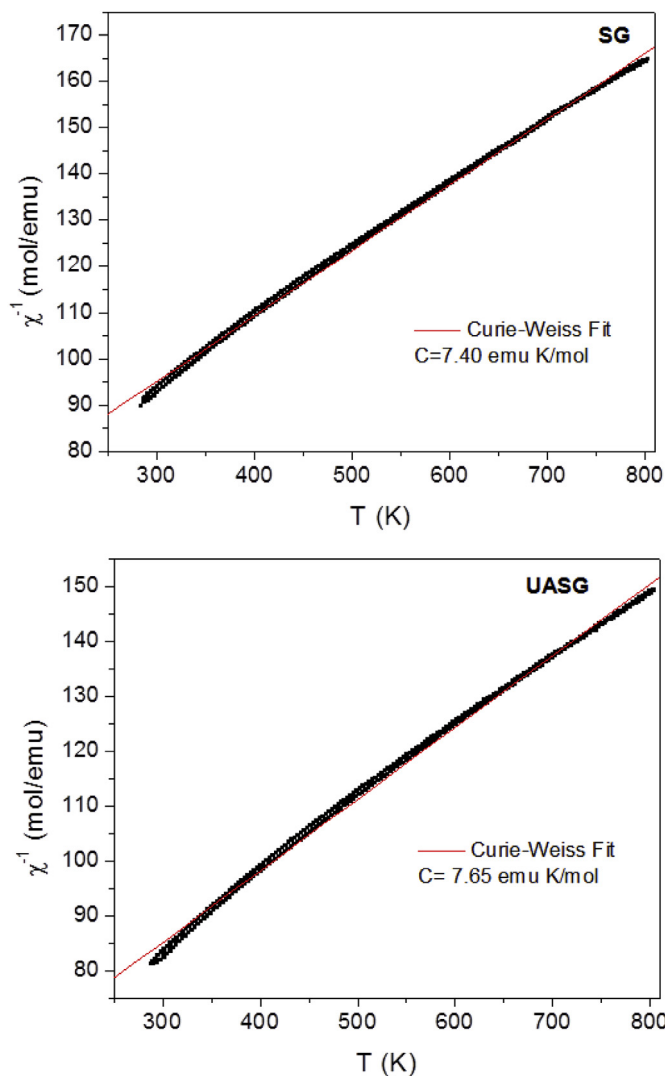
Fig. 6. Magnetic susceptibility vs. temperature plot at H = 5 KOe for samples prepared by SG and UASG methods.

Table 3
Experimental magnetic results. Effective magnetic moment, Molar Curie constant, Curie temperature, Curie−Weiss temperature

Sample	μ_{eff} (BM)	Cm (cm^3 K/mol)	T_C (K)	Θ (K)
SG	7.7	7.4	105	−245
UASG	7.8	7.7	103	−194

does not results especially clarifying: very different fitting models give place to very similar χ^2 values. Since in these samples we have performed other experimental characterizations (X-ray diffraction, magnetic measurements) which point out to the presence of Mn^{2+}, Mn^{3+} and Mn^{4+}, we have finally adopted a model that contemplates such a situation. That is, the Mn 3s spectra of the two samples have been fitted considering three doublets each one corresponding to a different manganese valence. In order to make the fitting procedure consistent we have used the following series of constraints:

- Same linewidth for all the peaks.
- ΔE_{3s} fixed, for the corresponding doublets, to the characteristic values of Mn^{2+}, Mn^{3+} and Mn^{4+} (see above)
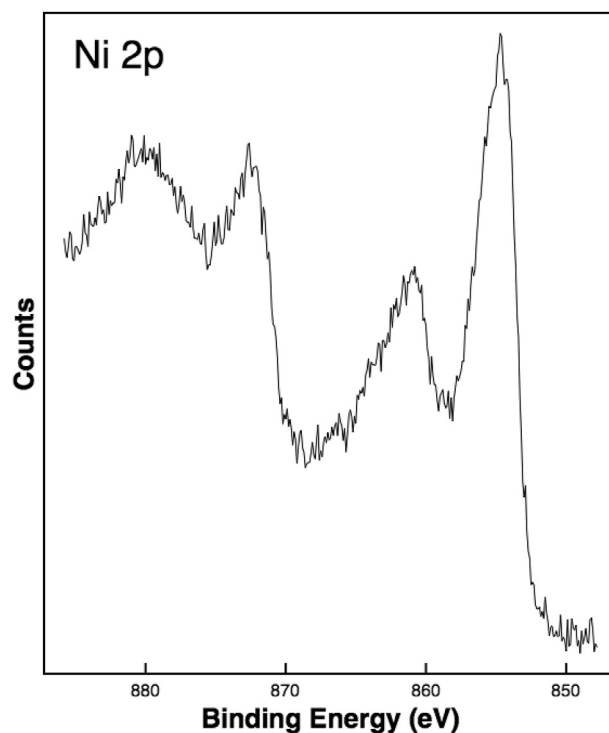

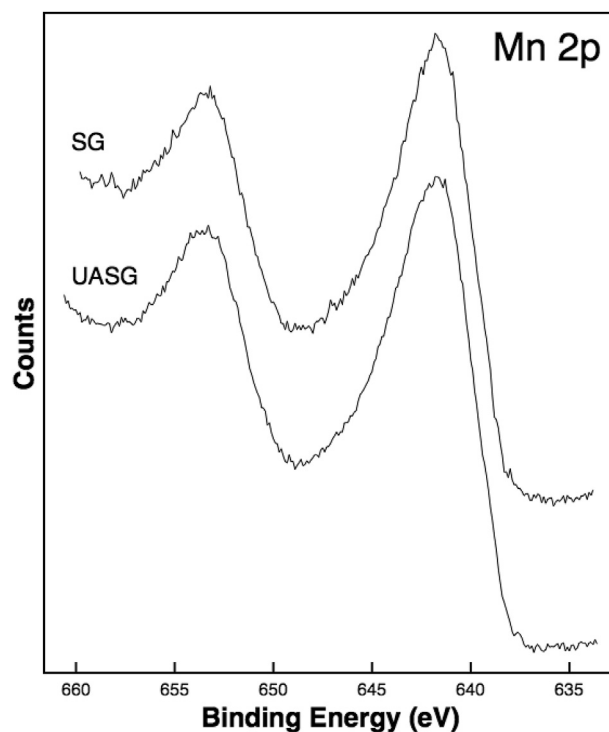**Fig. 7.** Ni 2p XPS spectrum recorded from the SG sample.

Fig. 8. Mn 2p XPS spectra recorded from both SG and UASG samples.

- The binding energy values for the Mn 3s(1) peak have been constrained to a range such that each of the contributions does not overlap with the following. That is, the positions of the Mn 3s(1) peaks have not been maintained fixed to the exact values
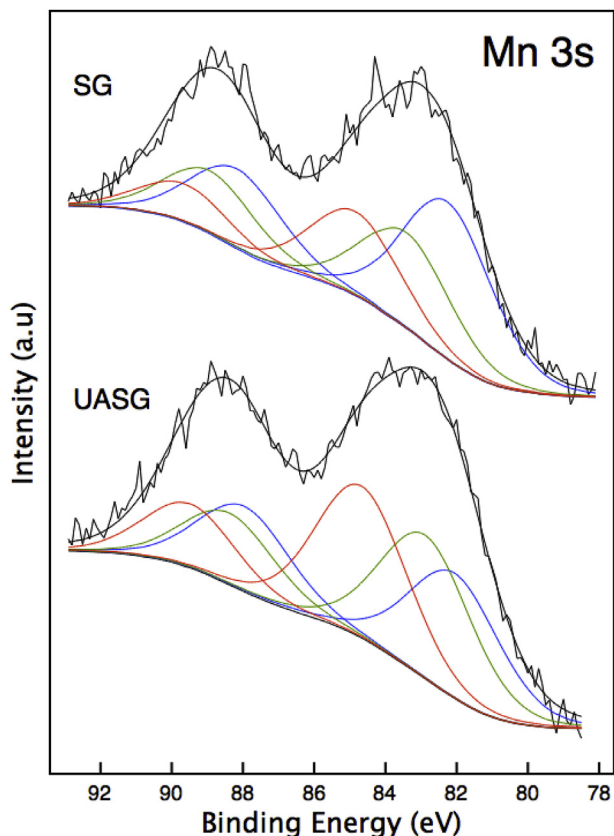
Fig. 9. Mn 3s XPS spectra recorded from the SG and UASG samples showing Mn^{2+}(blue), Mn^{3+} (green) and Mn^{4+} (red) contributions. (For interpretation of the references to colour in this figure legend, the reader is referred to the web version of this article.)

shown by the reference spectra, but we have allowed them to vary within reasonable intervals (± 0.3 eV) around these values.

- The area of the Mn 3s(2) peak was allowed to vary between the 40% and the 60% of the value of the area of the Mn 3s(1) peak since are these values the observed in the literature references.
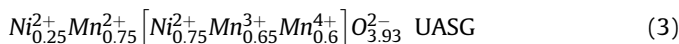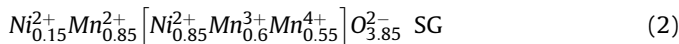
With all this, we have arrived to the results described in Fig. 9 and Table 4. It is interesting to note that If the average oxidation state of Mn is calculated from Table 4 taking into account the weight of the different Mn^{n+} contributions we obtain the values of 2.78 for the SG sample (which almost matches the value obtained from the Beyreuther equation) and 3.00 for the USAG sample which is within 4% the value obtained from the above-mentioned equation. The trend, besides, is consistent: Mn in the UASG sample shows a slightly higher oxidation state than Mn in the SG sample. However, and although the obtained values have a good level of consistence and plausibility, due to the limitations of the technique, they cannot be taken as totally definitive but as an indication of the weight due to the different contributions. The final cation distribution should take into account this information and that derived from the rest of the characterization techniques.

Table 4
Quantitative analysis of cations from XPS results for both preparations.

	Mn^{2+}	Mn^{3+}	Mn^{4+}
SG	0.91	0.62	0.47
Area (%)	45.5	31	23.5
UASG	0.66	0.67	0.67
Area (%)	32.8	33.5	33.7

3.5. Cation distribution

The Rietveld refinement of the XRD data corroborates that both samples crystallize in a cubic spinel structure (SG Fd3m). In order to determine the influence of the preparation method in the probable cation distribution, a crystallographic distribution was proposed for each oxide assuming that the ions Ni^{2+}, Mn^{2+}, Mn^{3+}, Mn^{4+} can be present according to their energetic preference to occupy the tetrahedral (Td) and octahedral (Oh) sites in the spinel structure [63–65]. To summarize the results obtained by crystallographic analysis, the cation distributions of this oxide $NiMn_2O_{4-\delta}$ as a function of synthesis method can be written as:

$$Ni^{2+}_{0.15}Mn^{2+}_{0.85}\left[Ni^{2+}_{0.85}Mn^{3+}_{0.6}Mn^{4+}_{0.55}\right]O^{2-}_{3.85} \quad \text{SG} \qquad (2)$$

$$Ni^{2+}_{0.25}Mn^{2+}_{0.75}\left[Ni^{2+}_{0.75}Mn^{3+}_{0.65}Mn^{4+}_{0.6}\right]O^{2-}_{3.93} \quad \text{UASG} \qquad (3)$$

As mentioned before, in both cases the compounds are non-stoichiometric in oxygen. A relative large inversion parameter ν of 0.85 (SG) and 0.75 (UASG) was found.

The oxide a-cell parameter can be estimated on the basis of the ion−oxygen bond length as a function of oxygen coordination using the relationship: $a = 2.0995\ \alpha + (5.8182\ \beta^2 - 1.4107\ \alpha^2)^{1/2}$ being $\alpha = \Sigma x_i (M_i\text{-O})_{Td}$ and $2\beta = \Sigma y_i (M_i\text{-O})_{Oh}$, where x_i and y_i are the stoichiometric coefficients, and $(M_i\text{-O})_{Td}$ and $(M_i\text{-O})_{Oh}$ are the tetrahedral and octahedral cation-oxygen distances, respectively. We have used the Shannon and Prewitt data [66] and Poix data [67] which consider the spin state and the preference of a cation for either site: Ni^{2+}-O_{Td} = 0.19, Mn^{2+}-O_{Td} = 0.2041, Ni^{2+}-O_{Oh} = 0.2047, Mn^{3+}-O_{Oh} = 0.205, Mn^{4+}-O_{Oh} = 0.1843 nm. The cell parameter value a calculated is compared with the experimental one to evaluate the validity of the cation distribution proposed.

The magnetically determined cation distribution was computed for each oxide from the best fit with the theoretical value of the molar Curie constant $Cm = \Sigma \nu_i C_i$ in with C_i is the individual ionic Curie constant, and the experimental ones obtained from the Curie−Weiss law. The individual ionic Curie values used were: $C_{Ni(II)}$ = 1, $C_{Mn(II)}$ = 4.22, $C_{Mn(III)}$ = 3, $C_{Mn(IV)}$ = 1.876 [68].

The values for the parameters calculated on the basis of the cation distributions obtained by Rietveld analysis are shown in Table 5. It can seen that the similarities of the observed and the calculated a, C_m, and z parameters validate the cation distributions I and II already proposed.

On the order hand, XPS analyses have showed that Ni^{2+}, Mn^{2+}, Mn^{3+} and Mn^{4+}-ions are present on the surface of both oxides. The relative quantity of Mn^{n+}-cations can be compared with those calculated from the cationic distributions. Table 6 shows a relatively good agreement. In fact, comparing the Mn-ions results obtained by XPS analyses with the concentration calculated for the same cations from the cation distributions, the results do not exceed 12% in Mn (II), 3% Mn (III) and 14% Mn (IV).

4. Conclusions

In this work we have proposed the cation distribution of the nickel manganite prepared using the sol−gel method and a novel ultrasound-assisted sol−gel method. The choice of a synthesis method for $NiMn_2O_{4-\delta}$ leads to particular structural parameters, magnetic properties and surface composition. The $NiMn_2O_{4-\delta}$ is non stoichiometric in oxygen, showing little variation of the cations concentration forming the oxide. The ultrasound method brings about a material showing a surface BET up to twelve times larger and a particle size up to 20% smaller than the material produced by the SG method. However, from the cation distribution point of view,

Table 5
Observed and calculated values of the lattice constants, a, molar Curie constant, Cm, and global charge, z, for both preparations.

$NiMn_2O_4$	a obs (A°)	a calc (A°)	Cm obs ($cm^3K\ mol^{-1}$)	Cm calc ($cm^3K\ mol^{-1}$)	z obs (eq.e/mol)	z calc (eq.e/mol)
SG	8.4090	8.4039	7.4	7.4	1.7	1.7
UASG	8.3969	8.3941	7.7	7.2	1.9	1.9

Table 6
Manganese concentrations from XPS results and from the cation distribution proposed.

XPS	Mn^{2+} (%)	Mn^{3+} (%)	Mn^{4+} (%)
SG	45.5	31	23.5
UASG	32.8	33.5	33.7
Cation distribution	Mn^{2+} (%)	Mn^{3+} (%)	Mn^{4+} (%)
SG	42.5	30	27.5
UASG	37.5	32.5	30

both methods lead to similar structures although the SG sample shows a higher concentration of Mn^{2+} and a slightly lower concentration of Mn^{4+}.

Acknowledgments

Appendix A. Supplementary data

Supplementary data related to this article can be found at http://dx.doi.org/10.1016/j.jallcom.2016.02.090.

References

[1] K.E. Sickafus, J.M. Wills, N.W. Grimes, Structure of spinel, J. Am. Chem. Soc. 82 (1999) 3279–3292.
[2] H.S.T.C. O'Neill, A. Navrotsky, Simple spinels, crystallographic parameters, cation radii, lattice energies and cation distribution, Am. Mineral. 68 (1983) 181–194.
[3] G. Blasse, Crystal chemistry and some magnetic properties of mixed metal oxides with spinel structure, Philips Res. Repts Suppl. 3 (1964) 1–139.
[4] B.P. Boucher, R. Buhl, M. Perrin, Étude crystallographique de manganite spinelle cubique $NiMn_2O_4$ par diffraction de néutrons, Acta Cryst. B 25 (1969) 2326–2333.
[5] B.P. Boucher, R. Buhl, M. Perrin, Structures magnétiques et étude des propriétés magnétiques des spinelles cubiques $NiMn_2O_4$, J. Phys. Chem. Solids 31 (1970) 363–383.
[6] B. Gillot, R. Legros, R. Metz, A. Rousset, Electrical conductivity of copper and nickel manganites in relation with the simultaneous presence of Mn^{3+} and Mn^{4+} ions on octahedral sites of spinel structure, Solid State Ionics 51 (1992) 7–9.
[7] A. Feteira, Negative temperature coefficient resistance (NTCR) ceramic thermistors: an industrial perspective, J. Am. Chem. Soc. 92 (2009) 967–983.
[8] C.H. Wu, J.S. Ma, C.H. Lu, Synthesis and characterization of nickel- manganese oxide via hydrothermal route for electrochemical capacitors, Curr. Appl. Phys. 12 (2012) 1190–1194.
[9] H. Pang, J. Deng, S. Wang, S. Li, J. Du, J. Chena, J. Zhanga, Facile synthesis of porous nickel manganite materials and their morphology effect on electrochemical properties, RSC Adv. 2 (2012) 5930–5934.
[10] J. Ponce, J.L. Rehspringer, G. Poillerat, J.L. Gautier, Electrochemical study of nickel-aluminium-manganese spinel $Ni_xAl_{1-x}Mn_2O_4$. Electrocatalytical properties for the oxygen evolution reaction and oxygen reduction reaction in alkaline media, Electrochim Acta 46 (2001) 3373–3380.
[11] G. Ashcroft, I. Terry, R. Grover, Study of the preparation conditions for $NiMn_2O_4$ grown from hydroxide precursors, J. Eur. Ceram. Soc. 26 (2006) 901–908.
[12] D. Fang, Z. Wang, P. Yang, W. Liu, C. Chen, A.J.A. Winnubst, Preparation of ultra-fined nickel manganite powders and ceramics by a solid-sate coordination reaction, J. Am. Ceram. Soc. 89 (2006) 230–235.
[13] S.M. Savic, M.V. Nikolic, O.S. Aleksic, M. Slankamenac, M. Zivanov, P.V. Nikolic, Intrinsic reactivity of sintered nickel manganite vs powder activation time and density, Sci. Sinter. 40 (2008) 27–32.
[14] R. Schmidt, A.W. Brinkman, Preparation and characterization of $NiMn_2O_4$ films, Int. J. Inorg. Mat. 3 (2001) 1215–1217.
[15] S. Iagtap, S. Rane, G. Gosavi, D. Amalnekar, Preparation, characterization and electrical properties of spinel-type environment friendly thick film NTC thermistors, J. Eur. Ceram. Soc. 28 (2008) 2501–2507.
[16] S. Asbrink, A. Waskowska, M. Drozd, E. Talik, Physical properties and X-ray diffraction of a $NiMn_2O_4$ single crystal below and above the ferromagnetic transition at Tc =145K, Phys. Chem. Solids 58 (1997) 725–729.
[17] A. Díez, R. Schmidt, A.E. Sagua, M.A. Frechero, E. Matesanz, C. Leon, E. Morán, Structure and physical properties of nickel manganite $NiMn_2O_4$ obtained from nickel permanganate precursor, J. Eur. Ceram. Soc. 30 (2010) 2617–2624.
[18] J.A. Aguilar-Garib, F. Sanchez-de-Jesús, A.M. Bolarín Miró, S. Ham- Hernández, Synthesis of $NiMn_2O_4$ assisted by high-energy ball milling of NiO-MnO powders, J. Ceram. Proc. Res. 12 (2011) 721–726.
[19] P. Duran, J. Tartaj, F. Rubio, O. Peña, C. Moure, Preparation and synthesis behaviour of the spinel-type $Co_xNiMn_{2-x}O_4$ (0.2≤x≤1.2) by the ethylene glycol-metal nitrate polymerized complex process, J. Eur. Ceram. Soc. 15 (2005) 3021–3025.
[20] P.B. Sinha, N.R. Sanjana, A.B. Biwas, On the structure of some manganites, Acta Cryst. 10 (1957) 439–440.
[21] M. O'Keeffe, Cation valencies and distributions in spinel structure containing manganese, J. Phys. Chem. Solids 21 (1961) 172–178.
[22] E.G. Larson, R.J. Arnott, D.G. Wickham, Preparation, semiconduction and low temperature magnetization of the system $Ni_{1-x}Mn_{2+x}O_4$, J. Phys. Chem. Solids 23 (1962) 1771–1781.
[23] B. Boucher, B.R. Buhl, M. Perrin, Neutron diffraction crystallography of cubic manganite spinel, $NiMn_2O_4$, Acta Cryst. Sect. B-Struct Crystal-logrCryst Chem. B 25 (1969) 2326–2333.
[24] G.T. Bhandage, H.V. Keer, Correlation of physical-properties of $Ni_xCu_{1-x}Mn_2O_4$ system, J. Phys. C Solid State Phys. 9 (1976) 1325–1330.
[25] A. Meenakshisundaram, N. Gunasekaran, V. Srinivasan, Distribution of metal ions in transition metal manganites AMn_2O_4 (A = Co, Ni, Cu or Zn), Phys. Status Solidi (a) 69 (1982) K15–K19.
[26] V.A.M. Brabers, J. Terhell, Electrical-conductivity and cation valencies in nickel manganite, Phys. Status Solidi (a) Appl. Res. 69 (1982) 325–332.
[27] V.A.M. Brabers, F.M. Vansetten, P.S.A. Knapen, X-ray photoelectron-spectroscopy study of the cation valencies in nickel manganite, J. Solid State Chem. 49 (1983) 93–98.
[28] E.D. Macklen, Electrical conductivity and cation distribution in nickel manganite, J. Phys. Chem Solids 47 (1986) 1073–1079.
[29] F. Golestani-Fard, S. Azimi, K.J.D. Mackenzie, Oxygen evolution during the formation and sintering of nickel manganese oxide spinels for thermistor applications, J. Mat. S. C. 22 (1987) 2847–2851.
[30] M.S. Islam, C.R.A. Catlow, Structural and electronic properties of $NiMn_2O_4$, J. Phys. Chem. Solids 49 (1988) 119–123.
[31] R. Legros, R. Metz, A. Rousset, Structural properties of nickel manganite $Ni_xMn_{3-x}O_4$ with 0.5≤ x ≤1, J. Mater S. C. 25 (1990) 4410–4414.
[32] B. Gillot, J.L. Baudour, K.F. Bouree, R. Metz, R. Legros, A. Rousset, Ionic configuration and cation distribution in cubic nickel manganites spinels $Ni_xMn_{3-x}O_4$ (0.57<x<1) in relation with thermal histories, Solid State Ionics 58 (1992) 155–161.
[33] T. Hashemi, A.W. Brinkman, X-ray photoelectron spectroscopy of nickel manganese oxide thermistors, J. Mat. Res. 7 (1992) 1278–1282.
[34] J.L. Baudour, F. Bouree, M.A. Fremy, R. Legros, A. Rousset, B. Gillot, Cation distribution and oxidation states in nickel manganites $NiMn_2O_4$ and $Ni_{0.8}Mn_{2.2}O_4$ from powder neutron diffraction, Phys. B Cond. Matter 180–181 (1992) 97–99.
[35] E. Elbadraoui, J.L. Baudour, C. Leroux, S. Fritsch, F. Bouree, B. Guillot, A. Rousset, Cation distribution, short range order, and small polaron hopping conduction in nickel manganites from neutron diffraction study, Phys. Stat. Solidi (b) 212 (1999) 129–139.
[36] J. Ponce, E. Ríos, J.L. Rehspringer, G. Poillerat, P. Chartier, J.L. Gautier, Preparation of nickel aluminium-manganese spinel oxides $Ni_xAl_{1-x}Mn_2O_4$ for oxygen electrocatalysis in alkaline medium: Comparison of properties stemming from different preparation methods, J. Solid State Chem. 145 (1999) 23–32.
[37] J.M.A. Almeida, C.T. Meneses, A.S. de Menezes, R.F. Jardim, J.M. Sasaki, Synthesis and characterization of $NiMn_2O_4$ nanoparticles using gelatin as organic precursor, J. Mag. Mag. Mat. 320 (2008) e304–e307.
[38] E.J.W. Verwey, Oxidic Semiconductors in Semi-conducting Materials, in: H.K. Henisch (Ed.), Butterworths Sc Pub Ltd, London, 1951, pp. 151–161.
[39] M.B. Wang, L. You, P. Ren, X. Yin, Y. Peng, B. Xia, L. Wang, X. Yu, S.M. Poh, P. Yang, G. Yuan, L. Chen, A. Rusydi, J. Wang, Oxygen-driven anisotropic transport in ultra-thin manganite films, Nat Commun. 4 (2013) 1–7.
[40] M.H. Ehsani, M.E. Ghazi, P. Kameli, F.S. Razavi, DC mangentization studies of nano- and micro-particles of bilayered manganite $LaSr_2Mn_2O_7$, J. Alloys Comp.

586 (2014) 261–266.

[41] P.N. Lisboa-Filho, M. Bahout, P. Barahona, C. Moure, O. Peña, Oxygen stoichiometry effects in spinel-type $NiMn_2O_{4-\delta}$ samples, J. Phys. Chem. Solids 66 (2005) 1206–1212.

[42] S.M. Savić, M. Tadić, Z. Jaglicić, K. Vojisavljević, L. Mancić, G. Branković, Structural, electrical and magnetic properties of nickel manganite obtained by a complex polymerization method, Ceram. Int. 40 (2014) 15515–15521.

[43] W. Vu, C.C. Forrington, F. Chapur, B. Dunn, Synthesis and Electrochemical Studies of Spinel Phase $LiMn_2O_4$ Cathode Materials Prepared by the Pechini Process, Electrochem Soc. 143 (1996) 879–884.

[44] H. Xu, B.W. Zeiger, K.S. Suslick, Sonochemical synthesis of nanomaterials, Chem. Soc. Rev. 42 (2013) 2555–2567.

[45] H.M.A. Rietveld, Profile refinement method for nuclear and magnetic structures, J. Appl. Cryst. 2 (1969) 65–71.

[46] J. Rodríguez-Carvajal, Recent advances in magnetic structure determination by neutronpowder diffraction, Phys. B 192 (1993) 55–69.

[47] D. Alburquenque, E. Vargas, J.C. Denardin, J. Escrig, J.F. Marco, J. Ortiz, J.L. Gautier, Physical and electrochemical study of cobalt oxide nano and microparticles, Mat. Charact. 93 (2014) 191–197.

[48] P.M.A. Sherwood, Practical Surface Analysis, in: second ed., in: D. Briggs, M.P. Seah (Eds.), Auger and X-ray Photoelectron Spectroscopy, Vol 1, Wiley, Chichester, 1990, p. 574.

[49] J. Faber, T. Fawcett, The powder diffraction file: present and future, Acta Cryst. B 58 (2002) 325–332.

[50] Y. Ma, M. Bathout, O. Peña, P. Durán, C. Moure, Magnetic properties of $(Co,Ni,Mn)_3O_4$ Spinels, Bol. Soc. Esp. Ceram. V43 (2004) 663–667.

[51] R.A. Ferreira, J.C.G. Tedesco, J.O. Birk, W. Kalcef, F. Yokaichiya, N. Rasmussen, O. Peña, P.F. Henry, G.G. Simeoni, H.N. Bordallo, P.N. Lisboa-Filho, Ferrimagnetism and spin excitation in a Ni–Mn partially inverted spinel prepared using a modified polymeric precursor method, Mat. Chem. Phys. 146 (2014) 58–64.

[52] B.B. Nelson-Cheeseman, R.V. Chopdekar, M.F. Toney, J.M. Iwata, E. Arenholz, Y. Susuki, Modified magnetic ground state in $NiMn_2O_4$ thin films, Phys. Rev. B 82 (2010) 14419–14427.

[53] Y. Shen, T. Nakayama, M. Arai, O. Yanawisawa, M. Izumi, Magnetic phase transition and physical properties of spinel-type nickel manganese, J. Phys. Chem. Solids 63 (2002) 947–950.

[54] M. Tadić, S.M. Savić, Z. Jaglicić, K. Vojisavljević, A. Radojiković, S. Prsić, D. Nikolić, Magnetic properties of $NiMn_2O_{4-\delta}$ (nickel manganite): Multiple

magnetic phase transitions and exchange bias effect, J Alloys Comp 588 (2014) 465–469.

[55] O. Peña, C. Moure, V. Bodenez, X. Cailleaux, B. Piriou, J. Ortiz, G. Zuñiga, J.L. Gautier, P.N. Lisboa-Filho, Magnetic properties of spinel-type oxides $NiMn_{2-x}Me_xO_4$, J. Chil. Chem. Soc. 50 (2005) 617–623.

[56] O. Peña, X. Cailleaux, B. Piriou, M. del Canto, S. Abarca, E. Ríos, J. Ortiz, J.L. Gautier, P.N. Lisboa-Filho, C. Moure, Magnetic properties of $Cu_{1+x}Mn_{2-x}O_4$ and $Ni_{1+x}Mn_{2-x}O_4$ solid solutions, J. Eur. Ceram. Soc. 27 (2007) 3911–3914.

[57] K. Maaz, A. Mumtaz, S.K. Hasanain, M.F. Bertino, Temperature dependent coercivity and magnetization of nickel ferrite nanoparticles, J. Mag. Mag. Mat. 322 (2010) 2199–2202.

[58] K.S. Kim, N. Winograd, X-ray photoelectron spectroscopic studies of nickel-oxygen surface using oxygen and argon ion-bombardment, Surf. Sci. 43 (1974) 625–643.

[59] J.L. Gautier, E. Ríos, M. Gracia, J.F. Marco, J.R. Gancedo, Characterisation by X-ray photoelectron spectroscopy of thin $Mn_xCo_{3-x}O_4(1 \geq x \geq 0)$ spinel films prepared by low-temperature spray pyrolysis, Thin Solid Films 311 (1997) 51–57.

[60] E. Beyreuther, S. Grafström, L.M. Eng, C. Thiele, K. Dörr, XPS investigation of Mn valence in lanthanum manganite thin films under variation of oxygen content, Phys. Rev. B 73 (2006) 155425–155429.

[61] N.V. Kosova, I.P. Asanov, E.T. Devyatkina, E.G. Avvakumov, State of Manganese Atoms during the Mechanochemical Synthesis of $LiMn_2O_4$, J. Solid State Chem. 146 (1999) 184–188.

[62] http://xpssimplified.com/elements/manganese.php.

[63] A. Navrotsky, O.J. Kleppa, The thermodynamics of cation distributions in simple spinels, J. Inorg. Nucl. Chem. 29 (1967) 2701–2714.

[64] L.E. Orgel, An Introduction to Transition-metal Chemistry. Ligand Field Theory, Methuen, 1966, p. 184.

[65] J.B. Goodenough, A. Casalot, P. Hagenmuller, Les oxides des métaux de transition, Gauthier-Villars, Paris, 1973.

[66] R.D. Shannon, C.T. Prewitt, Effective Ionic Radii in Oxides and Fluorides, Acta Cryst. B 25 (1969) 925–929.

[67] P. Poix, Sur une méthode de détermination des distances cation-oxygène dans les oxydes mixtes à structure spinelle. Application des valeurs à quelques cas particuliers, Bull. Soc. Chim. Fr. 5th Ser. 5 (1965) 1085–1087.

[68] B. Bleaney, B.I. Bleaney, Electricity and Magnetism, 3th Ed., Oxford University Press, 1976.